Azo(xy) *vs.* Aniline Selectivity in Catalytic Nitroarene Reduction by Intermetallics: Experiments and Simulations

Carena L. Daniels,[1] Da-Jiang Liu,[,2] Marquix A. S. Adamson,[1] Megan Knobeloch,[1] and Javier Vela*[,1,2]*

[1]Department of Chemistry, Iowa State University, Ames, Iowa 50011, United States, and [2]US DOE Ames Laboratory, Iowa State University, Ames, Iowa 50011, United States.

Corresponding Authors

* vela@iastate.edu

* dajiang@ameslab.gov

KEYWORDS. Intermetallic catalysts, nitroarene reduction, azoxyarenes, aniline, DeePMD simulations.

ABSTRACT. Intermetallic nanoparticles are promising catalysts in hydrogenation and fuel cell technologies. Much is known about the ability of intermetallic nanoparticles to selectively reduce

nitro, alkyne, alcohol, or halide functional groups; less is known about their selectivity toward aniline *vs.* azo or azoxy condensation products that result from reduction of a nitro group alone. Because azo(xy) arenes bear promise as dyes, chemical stabilizers, and building blocks to functional materials but can be difficult to isolate, developing high surface area, nanoparticle catalysts that display azo(xy) selectivity is desirable. To address this question, we studied a family of nanocrystalline group 10 metal (Pd, Pt)- and group 14 metal (Ge, Sn, Pb)-containing intermetallics—Pd_2Ge, Pd_2Sn, Pd_3Sn_2, Pd_3Pb, and PtSn—in the catalytic reduction of nitroarenes. In contrast to monometallic Au, Pt, and Pd nanoparticles, and "random" Pd_xSn_{1-x} nanoalloys, which are selective for aniline, atomically precise intermetallic nanoparticles of Pd_2Ge, Pd_2Sn, Pd_3Sn_2, and PtSn prefer an indirect condensation pathway and have a high selectivity for the azo(xy) products. The only exception is Pd_3Pb, the most active among the intermetallic nanoparticles studied here, which is instead selective for aniline. Employing a novel application of Molecular Dynamics—based on machine learned potentials within a DeePMD framework—to heterogeneous catalysis, we are able to identify key reaction species on the different types of catalysts employed, furthering our understanding of the unique selectivity of these materials. By demonstrating how intermetallic nanoparticles can be as active yet more selective than other more traditional catalysts, this work provides new physical insight and opens new opportunities in the use of these materials in other important chemical transformations and applications.

INTRODUCTION

Because of their unique catalytic activity, selectivity, and stability compared to their alloyed and monometallic counterparts,[1,2,3,4,5,6] atomically precise intermetallics are of interest in

industrially relevant processes ranging from fuel cell[7,8,9] to hydrogenation technologies.[10] Some of the most promising members of this family are binary 10-14 intermetallic nanoparticles composed of group 10 transition metals such as Pd and Pt and group 14 tetrel elements like Ge, Sn and Pb. For example, Pd_2Sn nanoparticles are active catalysts in the removal of nitrate from water,[11] ethanol oxidation,[12,13,14] oxygen reduction,[15] and H_2O_2 generation.[16] Pd_2Sn nanoparticles on Au are active in Sonogashira coupling, as well as in alkene and alkyne hydrogenation.[17] PdSn, Pd_3Sn_2, and Pd_2Sn nanoparticles chemoselectively hydrogenate crotonaldehyde, with PdSn nanoparticles having a high selectivity for the reduction of C=O *vs*. C=C bonds.[18] Catalytic Pd_3Sn_2 networks have been used in formic acid electrooxidation,[19] while Pd_2Ge nanoparticles are active in ethanol oxidation[20] and the hydrogen evolution reaction (HER).[21] Pd_3Pb nanoparticles are very active in the electrochemical reduction of oxygen,[22,23,24] of N_2 to NH_3,[25] and in the oxidation of formic acid,[26,27] ethanol[26,28] and various amines.[29,30] Pd_2Sn, Pd_2Ge, and Pd_3Pb nanoparticles are active in benzylamine oxidation.[30] PtSn nanoparticles are active in methanol electrooxidation,[31,32] furfural,[33] nitrobenzene, [34] styrene,[34] 3-nitrostyrene[35] and cinnamaldehyde[36] hydrogenation, and in the dehydrogenation of propane,[37] cyclohexane,[38] and *n*-butane.[38]

The reduction of nitroarenes—a primary method for synthesizing functionalized anilines that are widely used as pigments, pharmaceuticals, and agrichemicals—is a valuable test bed for intermetallic catalysts.[39] To date, a majority of studies in this area focused on a catalyst's ability to chemoselectively reduce the nitro group over other functional groups that may be present in the reactant, such as alkyne, alcohol, or halide.[18,35,40,41,42] Considerably less attention was paid to the catalyst's ability to chemoselectively reduce the nitro group into an aniline *vs.* the much less common azo or azoxy products—together termed “azo(xy)” compounds (Scheme 1). For

example, while Au nanoparticles supported on TiO_2 is selective toward anilines, changing the support to CeO_2,[42,43,44,45,46] hexagonal BN,[47] or polystyrene[48] shifts the selectivity toward azo(xy) arenes.[49] Other catalysts that favor azo(xy)arenes include Ni/graphene,[50] Pd/SiO_2,[51] Schiff base-modified nano Pt,[52] iron-/nitrogen-co-doped mesoporous carbon,[53] "single atom" Co,[54,55] and metal oxide catalysts.[56] Changing the solvent, reducing agent and temperature,[57,58,59,60] or employing a photo-[61,62,63,64,65] or electro-catalyst[66] can also affect the selectivity. Because azo(xy) arenes bear promise as dyes, chemical stabilizers, and building blocks to functional materials yet may be difficult to isolate, a better understanding of catalysts that display azo(xy) selectivity is desirable.[67,68,69,70,71] Therefore, unveiling the mechanistic factors behind the azo(xy) *vs.* aniline selectivity is important from both fundamental as well as practical perspectives.

Scheme 1. Different pathways for the reduction of nitroarenes.

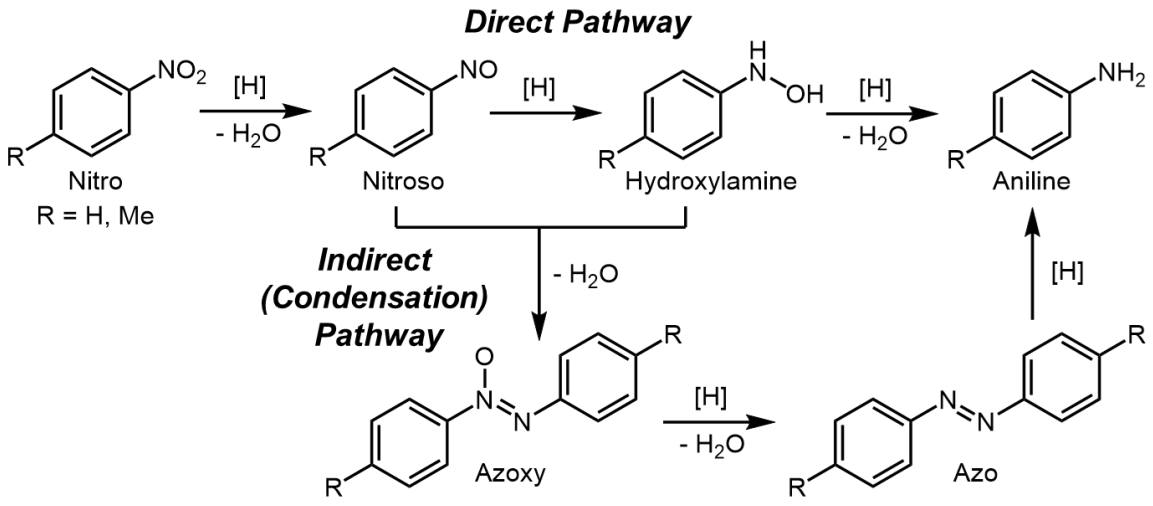

The two mechanistic pathways in Scheme 1 were originally proposed by Haber and are widely accepted today. In the direct pathway, the nitroarene is reduced to aniline through subsequent

nitrosoarene and hydroxylamine intermediates. Alternatively, two of these intermediates may react together *via* condensation to form an azoxyarene, which can be further reduced to an azoarene and, in some cases, aniline. In addition to the afore-mentioned experimental studies, the preference for direct *vs.* indirect pathways over single metals was studied by density functional theory (DFT).[72,73] Based on the calculated reaction and activation energies of each elementary step, the Ni(111)[72] and Pt(111)[73] surfaces were calculated to favor direct reduction under neutral conditions. However, on the Pt(111) surface, a change on the mode of reactant chemisorption from a flat to a tilted configuration rendered the indirect route's N-N coupling steps more favorable under basic conditions.[73]

Previously, we showed that an intermetallic Pd_2Sn nanocatalyst—made from a single source heterobimetallic precursor—is active in nitroarene reduction and has a unique selectivity for azoxyarenes, indicating a preference for the condensation pathway.[74] Here, we report a full account of the catalytic activity and selectivity of a wider family of 10–14 intermetallic, alloyed, and monometallic nanoparticles. In addition, for the first time, we use density functional theory calculations and machine learning-based *ab initio* molecular dynamics simulations to better understand the nitroarene reduction behavior of these nanomaterials. Our results provide a highly detailed picture of the catalytic activity and azo(xy) *vs.* aniline selectivity of nanoscale binary intermetallics.

METHODS

Materials. Sodium borohydride powder ($NaBH_4$, 98+%), 4-nitrotoluene (99%), and lead(II) bromide ($PbBr_2$, 98^+%) were purchased from Acros Organics; nitrobenzene (99%) from Oakwood Chemical; palladium (Pd, 99.95 %, 15 nm), platinum (Pt, 99.95%, 15 nm), and tin (Sn,

99.9%, 60-80 nm, metal basis) nanopowders from US Research Nanomaterials, Inc; palladium(II) bromide ($PdBr_2$, 99%), potassium tetrachloropalladate(II) (K_2PdCl_4, 99%), tin(II) chloride dihydrate ($SnCl_2 \cdot 2H_2O$, 98%), and gold nanoparticles on titania (1% Au/TiO_2) from Strem; carbon black (Vulcan XC-72R) from Fuel Cell Store; nitrosobenzene (>98.0%) from TCI America; 1-octadecene (ODE, technical grade, 90%), oleylamine (technical grade, 70%), oleic acid (technical grade, 90%), and ethylene glycol (99.8%, anhydrous) from Sigma Aldrich. Tax-free ethanol (200 proof) was sourced locally. All chemicals were used as received.

Synthesis of Intermetallic Nanocatalysts. Pd_2Sn, Pd_3Sn_2, Pd_2Ge, and PtSn nanocrystals were synthesized by the solid-state thermal decomposition of heterobimetallic pyridine-2-thiolate precursors.[74] In short, the relevant precursor was placed in an alumina combustion boat and was heated in a tube furnace under a N_2 atmosphere from 30 °C to 400 °C (or 600 °C in the case of Pd_3Sn_2) at a rate of 10 °C/min, and then allowed to cool to R.T. (25 °C). Pd_3Pb nanocubes were synthesized by the co-reduction of $PdBr_2$ and $PbBr_2$ with oleylamine and oleic acid in ODE at 170 °C for 30 min.[75]

Synthesis of Alloyed Pd_xSn_{1-x}/C Nanocatalysts. Alloyed Pd_xSn_{1-x}/C nanocatalysts with two different Pd:Sn ratios (x = 0.95 and 0.87) were prepared using a literature polyol method.[76] In summary, a stock solution of 12.5 mM Sn colloids was prepared by heating $SnCl_2 \cdot 2H_2O$ in a 12 mL solution of ethylene glycol and deionized water (11 mL and 1 mL, respectively) to 180 °C for 1 h. An aliquot of this stock solution (0.02 mmol, 1.6 mL for x = 0.95 or 0.06 mmol, 4.8 mL for x = 0.87) was diluted to 8 mL with ethylene glycol and heated to 130 °C under Ar. Upon reaching 130 °C, a solution of K_2PdCl_4 (0.08 mmol for x = 0.95 or 0.06 mmol for x = 0.87) in ethylene glycol was injected and the mixture was stirred at this temperature under Ar flow for 30 min. Upon cooling to R.T., the particles were deposited onto a carbon support by adding 25 mg

of Vulcan XC-72R and stirring at a rate of 600 rpm at R.T. for 1 h. The particles were washed with ethanol and acetone, dried under vacuum, and placed under Ar/H_2 flow in a tube furnace for 1 h at 205 °C. %Sn content was calculated using the (111) reflection shifts relative to the Pd (0% Sn) and Pd_3Sn (25% Sn) fcc standard patterns.

Characterization. Powder XRD was collected on a Rigaku Ultima IV diffractometer with a Cu Kα radiation source (40 kV, 44 mA). 2-5 mg per sample was smeared onto a backgroundless quartz slide. For alloy characterization, 1-10%$^{w}/_{w}$ Si powder was added as an internal standard.

Catalytic Reduction Experiments. Nitroarene (0.1 mmol of nitrobenzene or p-nitrotoluene) or nitrosobezene (0.1 mmol), ethanol (2.00 mL), nanocatalyst (10 mg), and $NaBH_4$ (0.6 mmol) were placed in a 5 mL vial. The mixture was stirred for 48 h. Small aliquots (0.50 mL) were taken at specific intervals, filtered, and consistently diluted for analysis by gas chromatography-mass spectroscopy (GCMS), on an Agilent 7250 GC-QTOF.

Ab Initio Molecular Dynamics Simulations/DFT Calculations. To gain insights into mechanism of nitrobenzene hydrogenation, we performed *ab initio* Molecular Dynamic (MD) simulations with DFT. The main features of the simulations are: (1) 4 nitrobenzene, 4 ethanol, and 48 hydrogen molecules in a simulation box with periodic boundary conditions. (2) Catalysts are simulated by a nanocluster of 10 or 20 atoms for Au and Pt, and 12 or 24 atoms for Pd_2Sn NC. (3) MD simulations using NVT ensemble. To obtain reactions in a feasible time scale, simulations were performed at elevated temperature and pressure, typically from 1000 K to 2000 K, and between 10 to 50 kBar, and for 10 ps. Simulation results are then analyzed by a home-made Python software with extensive use of the ASE (Atomic Simulation Environment) package. Specifically, we use ASE to construct an adjacency matrix and then use breadth-first search algorithm to find individual molecules. For systems with catalysts, we removed the

catalyst from the system first. At this stage, we only identified the resulting molecules using the molecular formula and manually examined and identified selected examples. We note that a similar and somewhat more sophisticated code tailored for MD simulations using ReaxFF has been developed.[77]

RESULTS AND DISCUSSION

Intermetallic Nanocatalysts and Benchmarks. To better understand the unique catalytic behavior of intermetallic nanocatalysts, a family of binary 10–14 intermetallic nanocrystals—Pd_2Ge, Pd_2Sn, Pd_3Sn_2, Pd_3Pb, and PtSn (Figures 1 and 2)—were synthesized and tested for the catalytic reduction of nitroarenes (see Supporting Information (SI) and Methods). All intermetallic nanophases were characterized by powder X-ray diffraction (Figure 1). Average single crystalline domain (Scherrer) sizes remained 12–51 nm in all cases. While this family encompasses a variety of structure types, it provides a diverse platform to compare how each nanocatalyst behaves based on the presence of differing transition metals (Pd, Pt), group 14 elements or "tetrels" (Ge, Sn, Pb), and metal–to–tetrel content (Pd_2Sn, Pd_3Sn_2). For comparison, monometallic nanoparticles of Pd, Pt, and Sn available commercially were also tested as catalysts for the same transformation. Powder X-ray diffraction of these samples showed relatively phase pure Pd and Pt nanoparticles with Scherrer sizes ranging from 5–16 nm, while Sn nanoparticles had a Scherrer size of about 55 nm and a small amount (~8%) of SnO impurity. As an additional benchmark and to address the possible effect(s) of structure as well as composition on catalysis, we also tested Pd_xSn_{1-x}/C alloyed nanoparticles made through a modified polyol approach (see SI).[76] Analyses of referenced peak shifts and peak widths show compositions of $Pd_{0.95}Sn_{0.05}$/C and $Pd_{0.87}Sn_{0.13}$/C and Scherrer sizes of 8–10 nm (Figure 3).

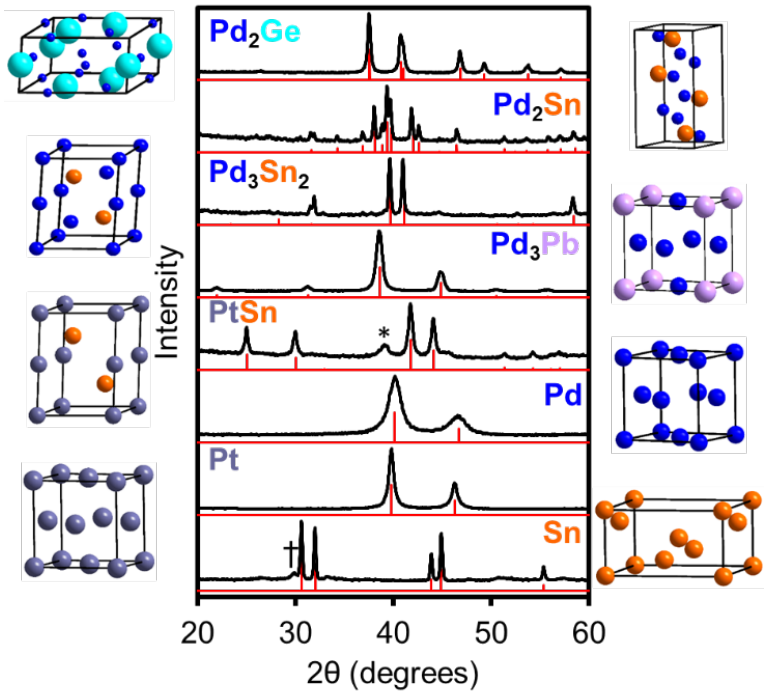

Figure 1. Powder XRD and corresponding unit cells of 10–14 intermetallic nanoparticles and monometallic nanocatalysts tested against nitroarene reduction. Standard patterns are shown in red: Pd_2Sn, orthorhombic, Pnma, ref. 158364; Pd_3Sn_2, hexagonal, $P6_3/mmc$, ref. 197134; Pd_2Ge, hexagonal, P-62m, ref. 76140; Pd_3Pb, cubic, Pm-3m, ref. 42600; PtSn (* = Pt_3Sn, 1%), hexagonal, $P6_3/mmc$, ref. 42593; Pd, cubic, Fm-3m, ref. 52251; Pt, cubic, Fm-3m, ref. 243678; β-Sn († = SnO, 8%), tetragonal, $I4_1/amd$, ref. 252800.[78] XRD data for Pd_2Ge, Pd_2Sn, Pd_3Sn_2, and PtSn nanoparticles was adapted with permission from Daniels, C. L.; Knobeloch, M.; Yox, P.; Adamson, M. A. S.; Chen, Y.; Dorn, R. W.; Wu, H.; Zhou, G.; Fan, H.; Rossini, A. J.; Vela, J. Intermetallic Nanocatalysts from Heterobimetallic Group 10−14 Pyridine-2-Thiolate Precursors. *Organometallics* **2020**, *39*, 1092−1104. Copyright 2020 American Chemical Society.[74] Of these, only Pd_2Sn was previously employed in a preliminary study of nitrobenzene hydrogenation.[74]

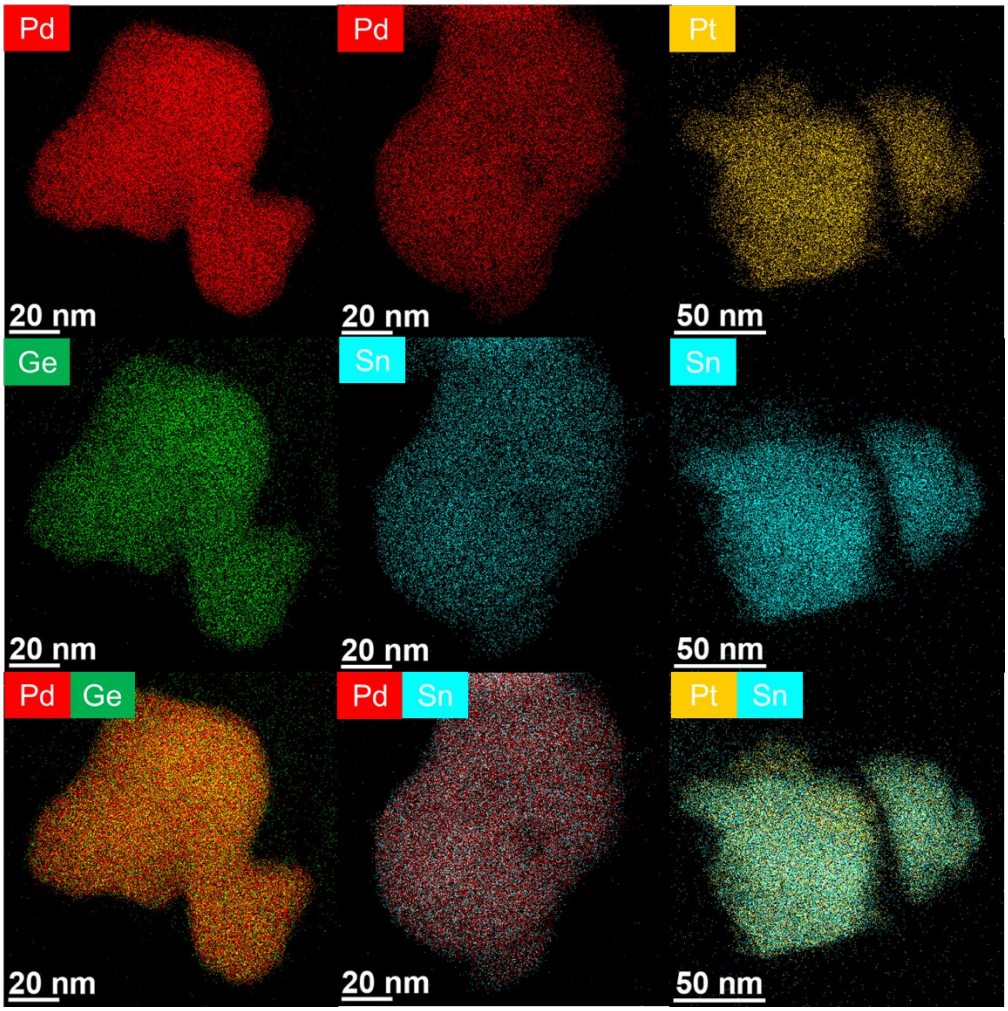

Figure 2. EDX elemental mapping of the intermetallic Pd_2Ge, Pd_2Sn, and PtSn nanoparticles (additional TEM data is available in the Supporting Information).

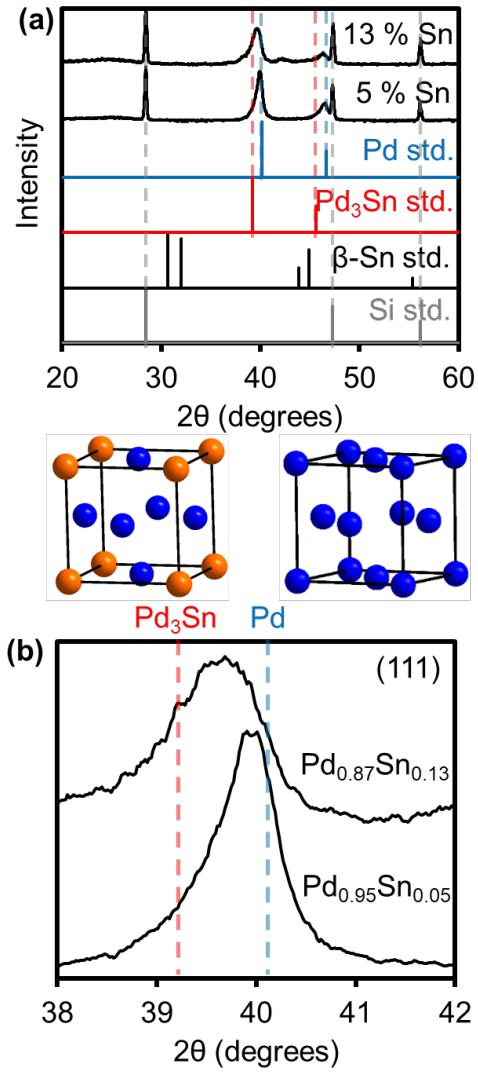

Figure 3. (a) Powder XRD patterns of alloyed Pd_xSn_{1-x}/C nanoparticles. Reflections shift to lower 2θ values upon Sn incorporation. Because β-Sn's tetragonal structure ($I4_1/amd$) is different to that of fcc Pd ($Fm\text{-}3m$), the pattern for the binary intermetallic nanophase Pd_3Sn—which does adopt a topologically similar structure to Pd—was used as a surrogate for a hypothetical nanoalloy with a reference Sn content of 25% (*i.e.*, $Pd_{0.75}Sn_{0.25}$). A small amount (1-10% $^{w}/_{w}$) of powdered crystalline silicon was used as an internal standard. (b) (111) reflection.

Nitrobenzene Reduction. An ethanol solution of nitrobenzene and $NaBH_4$—a conveniently safer surrogate for H_2[79]— undergoes no appreciable change at room temperature (R.T., 25 °C) for at least 48 h (Scheme 2). In contrast, nitrobenzene is reduced to aniline in as little as 4 h in the presence of a suitable nanocatalyst such as titania-supported nano gold (Au/TiO_2, Figure 4).[74,79] Under identical conditions—ethanol, R.T.—Pd_2Ge nanoparticles are less active but have different selectivity, with azoxybenzene being the main observed product after 48 h (Table 1). When Pd_2Sn nanoparticles are used, nitrobenzene is reduced in 8 h, at which time the major product is also azoxybenzene;[74] interestingly, longer reaction times lead to a decrease in the concentration of azoxybenzene and a concomitant increase in the concentration of azobenzene, with the latter becoming the sole product after 48 h. A similar behavior is observed with Pd_3Sn_2 nanoparticles; however, in this case both azobenzene and aniline begin to appear after 24 h and 48 h, respectively—see SI. In comparison, Pd_3Pb nanoparticles are very active, with nitrobenzene being reduced almost completely in just 1 h (Figure 4); in this case, neither azoxybenzene or azobenzene is observed, with the sole product being aniline. PtSn nanoparticles are behave similarly to Pd_2Sn nanoparticles, but achieve lower nitrobenzene conversion; in this case, azoxybenzene and azobenzene start to appear at 4 h, with azobenzene becoming the major product at 48 h.

Scheme 2. Catalytic reduction of nitrobenzene and nitrosobenzene.

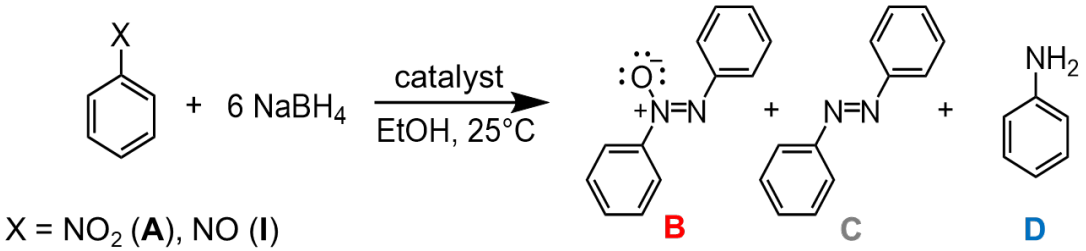

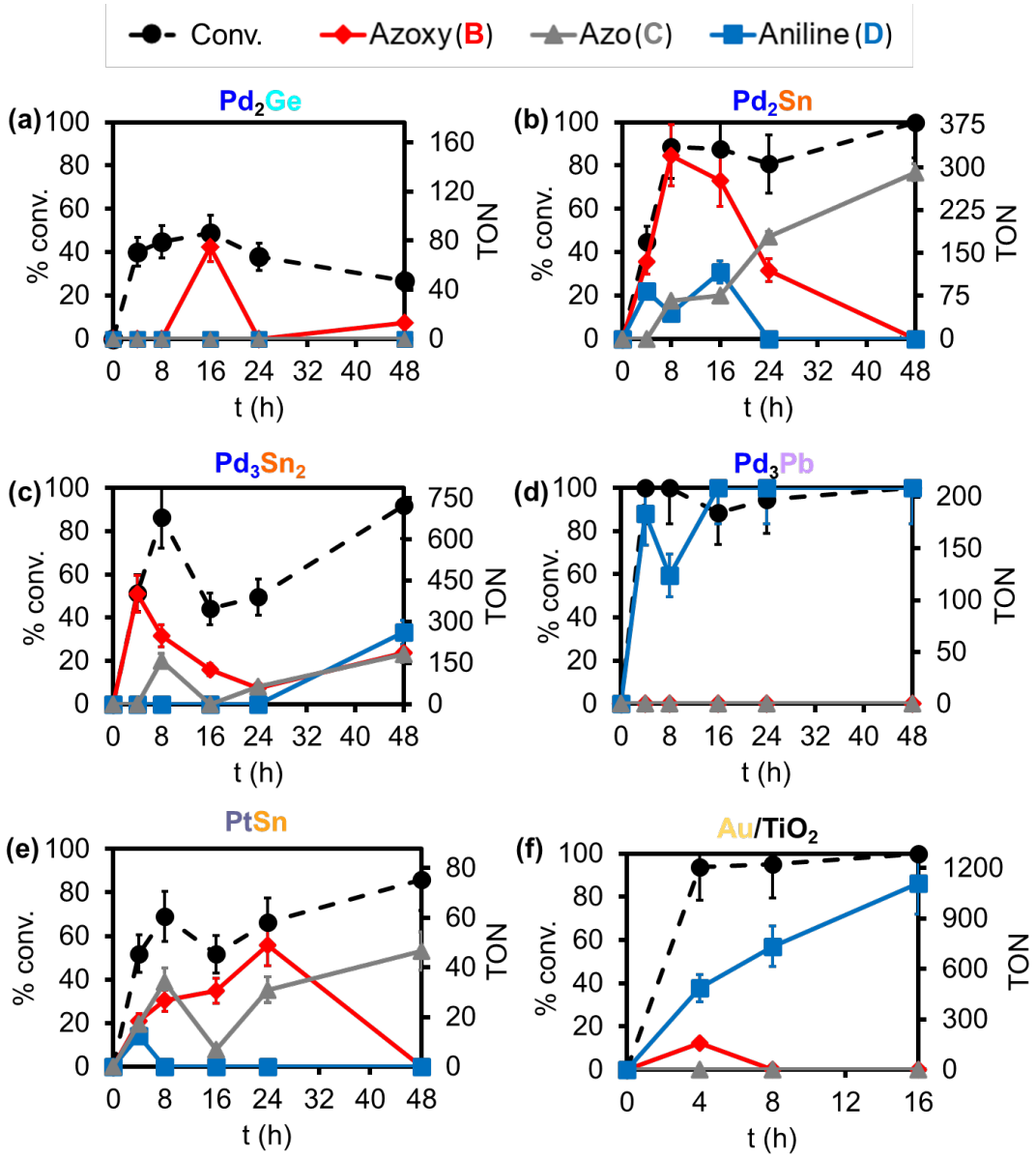

Figure 4. Representative examples of nitrobenzene reduction over intermetallic 10–14 nanoparticle catalysts (a) Pd_2Ge, (b) Pd_2Sn, (c) Pd_3Sn_2, (d) Pd_3Pb, (e) PtSn, *vs.* monometallic nanoparticle catalyst (f) Au/TiO_2 (0.1 mmol nitrobenzene, 0.6 mmol $NaBH_4$, 10 mg catalyst, 2 mL ethanol, 25 °C, see Methods). The standard deviation of conversion measurements obtained from multiple runs across all catalyst types averaged 11%.

Table 1. Representative nitro- ($PhNO_2$, **A**) and nitroso-benzene (PhNO, **I**) reduction data using binary 10–14 intermetallic nanoparticles *vs.* monometallic and alloyed Pd_xSn_{1-x}/C nanocatalysts.[a]

Nanocatalyst (Size nm[b])	Reactant	Time (h)	Conv.[c] (%)	TON[d] (TOF[e] / h)	Selectivity[f] (%)		
					Azoxy (**B**)	Azo (**C**)	Aniline (**D**)
None (control)	$PhNO_2$ (**A**)	48	0	0 (0)	0	0	0
	PhNO (**I**)	4	>99	N/A	>99	0	0
		48	>99	N/A	80	20	0
Au/TiO_2[g] (1 wt% Au, 4.4)	$PhNO_2$ (**A**)	4	94	1210 (302)	25	0	75
		16	>99	1287 (80.4)	0	0	>99
	PhNO (**I**)	1	>99	1287 (1287)	10	41	48
		48	>99	1287 (26.8)	0	30	70
Pd_2Ge[h] (28 ± 7)	$PhNO_2$ (**A**)	4	40	70.5 (17.6)	0	0	0
		48	27	47.7 (0.994)	>99	0	0
Pd_2Sn[h] (49 ± 11)	$PhNO_2$ (**A**)	4	45	171 (42.7)	62	0	38
		48	>99	378 (7.88)	0	>99	0
	PhNO (**I**)	1	>99	378 (378)	54	46	0
		48	>99	378 (7.88)	0	>99	0
Pd_3Sn_2[h] (51 ± 7)	$PhNO_2$ (**A**)	4	51	402 (101)	>99	0	0
		48	92	725 (15.1)	30	29	42
Pd_3Pb[75] (12 ± 1)	$PhNO_2$ (**A**)	1	93	194 (194)	0	0	>99
		2	>99	208 (104)	0	0	>99
PtSn[h] (24 ± 4)	$PhNO_2$ (**A**)	4	52	45.6 (11.4)	38	36	26
		48	86	75.4 (1.57)	0	>99	0
Pd[g] (5 ± 1)	$PhNO_2$ (**A**)	1	89	8.09 (8.09)	0	0	>99
		4	>99	9.09 (2.27)	0	0	>99
Pt[g]	$PhNO_2$ (**A**)	1	49	26.1 (26.1)	78	0	22

(16 ± 1)		48	95	50.5 (12.6)	2.5	6.9	91
β-Sn[g]	$PhNO_2$ (**A**)	4	82	61.2 (15.3)	>99	0	0
(55 ± 6)		48	95	70.9 (1.48)	0	33	67
$Pd_{0.95}Sn_{0.05}/C$[76]	$PhNO_2$ (**A**)	48	>99	19.3 (0.400)	0	0	>99
(10 ± 2)							
$Pd_{0.87}Sn_{0.13}/C$[76]	$PhNO_2$ (**A**)	48	91	15.4 (0.320)	0	>99	>99
(8 ± 1)							

[a]10 mg nanocatalyst, 0.1 mmol reactant, 0.6 mmol $NaBH_4$, 2 mL ethanol, 25 °C (see Methods). [b]Single crystalline domain (Scherrer) size in nm. [c]The standard deviation of conversion measurements obtained from multiple runs across all catalyst types averaged 11%. [d]TON = moles of converted reactant / moles of individual (per atom) surface active nanocatalyst sites. [e]TOF = TON / time. [f]Determined by GC-MS. [g]Commercial. [h]This work and ref. 74.

Effect of Intermetallic Nanoparticle Composition. In the nitrobenzene reduction experiments with intermetallic nanoparticle catalysts, the observed turnover numbers (TONs) of 725–45.6 are all significantly larger than one (>>1), which attests to the true catalytic nature of these nanomaterials (Table 1). The intermetallic nanocatalysts show maximum turnover frequencies (TOF_{max}) of 194–11.4 h^{-1} (Table 1, Figure 5); these are not far behind that observed for nano Au/TiO_2 of 302 h^{-1}, the most active among the literature benchmarks used here. The intermetallic nanoparticle TOF_{max} values are 1-2 orders of magnitude larger than those observed for unsupported monometallic nanocatalysts, 26.1–8.09 h^{-1}; they are also 3 orders of magnitude larger than those observed for alloyed Pd_xSn_{1-x}/C nanocatalysts, 0.400–0.320 h^{-1} (see below). Among intermetallic nanocatalysts, Pd_2Ge nanoparticles display modest activity, with a TOF_{max} of 17.6 h^{-1}, and 27% conversion after 48 h; at this time, azoxybenzene is the only product detected, indicating that the reduction reaction over Pd_2Ge nanoparticles follows the condensation pathway (Scheme 1). Pd_2Sn and Pd_3Sn_2 nanoparticles are both more active than

Pd_2Ge nanoparticles, with TOF_{max} values of 42.7 h^{-1} and 101 h^{-1}, respectively, and >99%–92% conversion after 48 h (Figure 5). This suggests that, for a given transition metal, Sn is a more active tetrel than Ge. Interestingly, while the reactions with both Pd_2Sn and Pd_3Sn_2 nanoparticles also follow the condensation pathway, each nanocatalyst exhibits different selectivity. At 48 h, Pd_2Sn nanoparticles are selective for azobenzene, while Pd_3Sn_2 nanoparticles give a mixture of all possible products, with aniline being the most abundant (Figures 4 and 5, Table 1). This suggests that the reduction of azobenzene to aniline is more favorable for Pd_3Sn_2 than Pd_2Sn nanoparticles, and that this step is faster than the reduction of azoxybenzene to azobenzene with Pd_2Sn nanoparticles. When the reaction is carried out with *p*-nitrotoluene instead of nitrobenzene, the same patterns are observed, except that the reaction proceeds beyond the azo reduction step (see SI). This suggests that the more electron-rich reactant 4,4'-azotoluene is more easily reduced than azobenzene. The reduction of nitrobenzene over PtSn nanoparticles is similar to that over Pd_2Sn than Pd_3Sn_2 nanoparticles, where the only product observed at 48 h is azobenzene. Therefore, the PtSn nanoparticles also prefer the condensation pathway; however, PtSn nanoparticles are less active, with a TOF_{max} of 11.4 h^{-1}, and 86% conversion after 48 h (Table 1 and Figure 5).

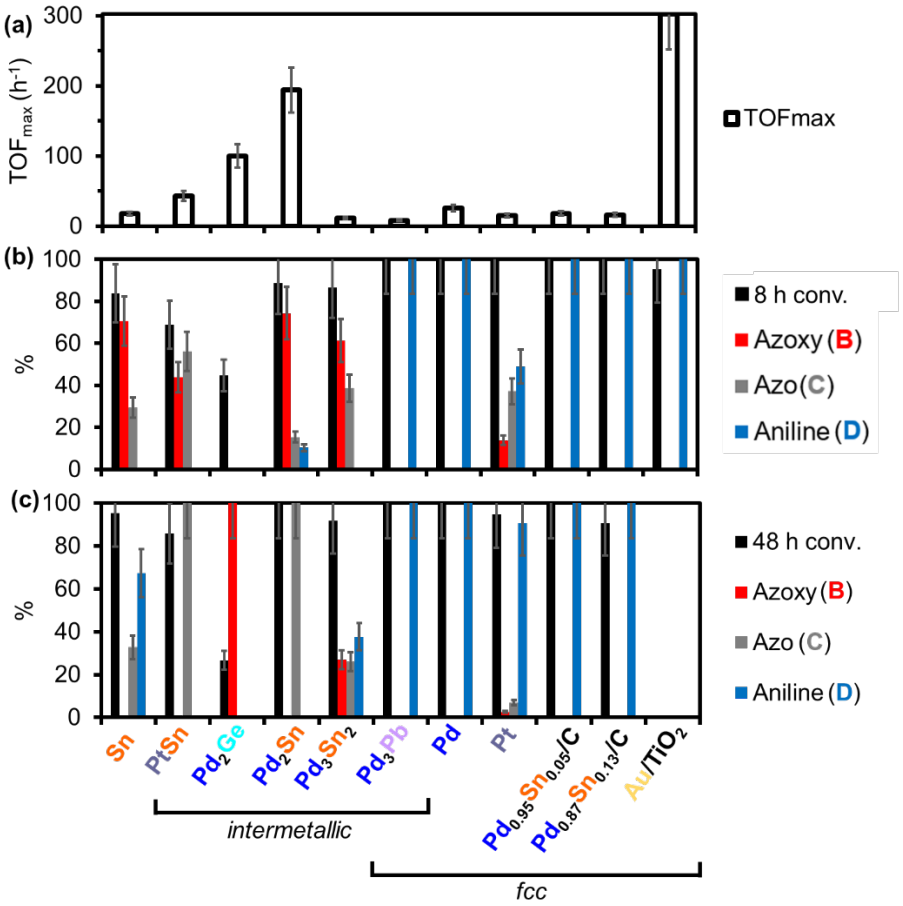

Figure 5. Representative activity and selectivity data for the catalytic reduction of nitrobenzene over binary 10–14 intermetallic nanoparticles, monometallic nanoparticles, and Pd_xSn_{1-x}/C nanoalloys (0.1 mmol nitrobenzene, 0.6 mmol $NaBH_4$, 10 mg nanocatalyst, 2 mL ethanol, 25 °C, see Methods). (a) TOF_{max} (4 h data for Pd_2Ge, Pd_2Sn, Pd_3Sn_2, PtSn, Sn, and Au/TiO_2, and 1 h data for Pd_3Pb, Pd, Pt, $Pd_{0.95}Sn_{0.05}$/C and $Pd_{0.87}Sn_{0.13}$/C), % conversion and product selectivities at (b) 8 h and (c) 48 h. The standard deviation of conversion measurements obtained from multiple runs across all catalyst types averaged 11%.

In contrast to the other intermetallic nanoparticle catalysts studied here, we note that Pd_3Pb nanoparticles show a preference for the direct rather than the condensation pathway (Scheme 1).

In fact, azoxy or azo intermediates remain undetected during the progress of the reaction when this nanocatalyst is used. The activity of Pd_3Pb nanoparticles is significantly higher compared to that of Ge- and Sn-based intermetallic nanoparticles; their TOF_{max} is 194 h^{-1}, with 1 h and 2 h conversions of 93% and >99%, respectively (Table 1). Overall, moving down group 14—as the tetrel gets heavier—generally increases the catalytic activity,[1,10,28,29] with noticeable effects also on each of the nanocatalysts' selectivity.

Comparison to Single Metal Nanoparticles and Nanoalloys. In addition to the literature catalyst nano Au/TiO_2[79]—see above—we also studied nitrobenzene reduction catalyzed by monometallic Pd, Pt, and Sn nanoparticles obtained commercially. Among these unsupported catalysts, Pt nanoparticles are the most active with a TOF_{max} of 26.1, and >99% conversion within 4 h (Table 1). The reduction of nitrobenzene over both Pt and Sn nanoparticles favors the condensation pathway, as indicated by the presence of azoxy and azo intermediates throughout the reaction (Table 1). In both Pt and Sn nanoparticle cases, aniline is the major product after 48 h, showing that both metals are able to reduce azobenzene to aniline. Pt nanoparticles are slightly better at this step than Sn nanoparticles, with an aniline selectivity at 48 h of 91% and 67%, respectively (Figure 5). In contrast to monometallic Pt or Sn nanoparticles, no intermediates are observed during nitrobenzene reduction over Pd nanoparticles, indicating the latter prefer the direct pathway. This strongly indicates that the presence of the group 14 (tetrel) element—Ge, Sn, Pb—in the intermetallic nanoparticles affects the activity and—in the case of Ge and Sn, but not Pb nanoparticles—the preferred pathway and selectivity of the reaction.

To probe the effect of nanoparticles atomic structuring on catalytic behavior, we tested disordered—also called "random"— Pd_xSn_{1-x} nanoalloys as catalysts for nitrobenzene reduction. While these only reach limited TOF_{max} values of 0.400–0.320, they otherwise behave similar to

monometallic Pd nanoparticles, with 48 h conversions of >99% and 91% for $Pd_{0.95}Sn_{0.05}$ and $Pd_{0.87}Sn_{0.13}$ nanoalloys, respectively (Figure 5). Both nanoalloy catalysts are selective for aniline, with no azo(xy) intermediates observed throughout the reaction. This indicates that the reaction over these catalysts follows the direct pathway, as it does with Pd nanoparticles. Further, as observed for Pd-Sn nanoparticle intermetallics, the specific Sn content affects the catalytic activity, because both nanoalloys and intermetallic nanoparticles with lower Sn content show higher conversion. However, unlike Pd-Sn intermetallic nanoparticles, Sn content does not appear to impact the selectivity of the Pd_xSn_{1-x} nanoalloys. Together, these observations strongly indicate that atomic ordering has a significant impact in catalysis by intermetallic nanoparticles.

Nitrosobenzene Reduction. To gain deeper insight into the mechanism of the catalytic reaction, we replaced the reactant with nitrosobenzene, a possible intermediate of nitrobenzene reduction (**I** in Scheme 1). In this case, even in the absence of a catalyst, nitrosobenzene is rapidly reduced by $NaBH_4$ to azoxybenzene (Scheme 2, Figure 6). However, after this initial reduction, only a small amount of azoxybenzene is converted to azobenzene, and the azoxybenzene to azobenzene ratio levels off at *ca.* 4:1 after 48 h (Figure 6). In contrast, in the presence of Pd_2Sn, the azoxybenzene is fully converted to azobenzene after 8 h (Figure 6b), demonstrating once more the impact of the Pd_2Sn intermetallic nanoparticle on the chemoselectivity of the reaction. This experiment supports the observation that nitrobenzene reduction over Pd_2Sn nanoparticles almost exclusively follows the condensation pathway, with Pd_2Sn nanoparticles being very active for the conversion of azoxybenzene to azobenzene but not as active for the sequential reduction of azobenzene to aniline. When Au/TiO_2 is used as catalyst, nitrosobenzene reduction results in ~50% aniline, ~40% azobenzene and very minimal ~10% azoxybenzene in 1 h. After 48 h, azoxybenzene disappears and the aniline to azobenzene ratio levels off at *ca.* 7:3 (Figure 6c).

This reveals both the direct and indirect condensation pathways are followed with Au/TiO_2, with the latter getting inhibited after the azobenzene reduction step. While more aniline is produced with Au/TiO_2, higher selectivity is observed for intermetallic Pd_2Sn nanoparticles.

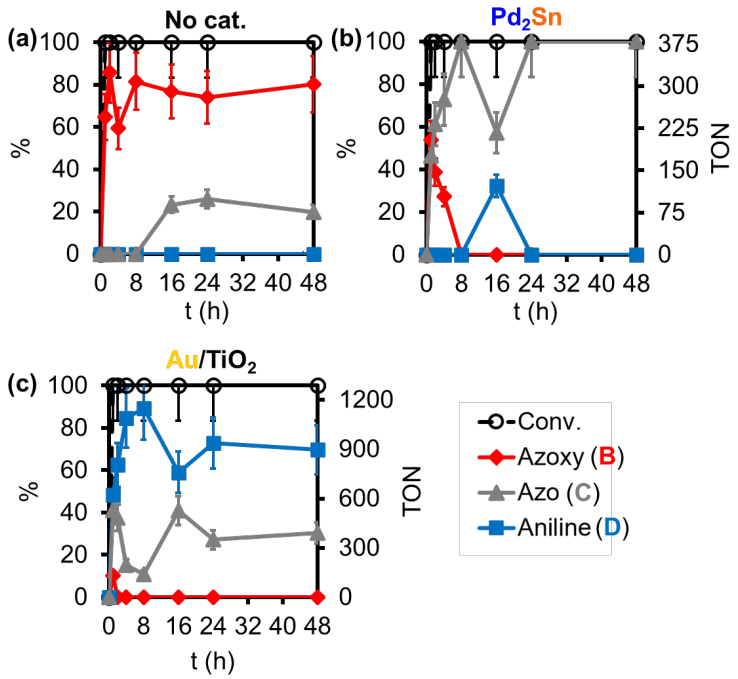

Figure 6. Reduction of nitrosobenzene (a) without a catalyst, (b) over Pd_2Sn nanoparticles, and (c) over Au/TiO_2. TON not calculated for (a) because no catalyst was used. The standard deviation of conversion measurements obtained from multiple runs across all catalyst types averaged 11%.

Nanoreactor Simulations. We first attempted to elucidate the selectivity for nitroarene reduction on intermetallic nanoparticle catalysts using standard "static" DFT analysis of reactant configuration energetics on perfect low-index single-crystal surfaces. However, these surfaces do not necessarily reflect relevant catalyst configurations. Furthermore, this is not a viable way to

successfully probe the large configurational phase space to extract relevant catalytic pathways and energetics.

Instead, Molecular Dynamics (MD) simulations with reliable interactions, *e.g.*, obtained from Density Functional Theory (DFT), provide a way to address this challenge. Indeed, our *ab initio* MD simulations have allowed us to identify a phenylamino radical (C_6H_5N•) as an important reaction intermediate on the Pd_2Sn nanocatalyst (see details in Methods). In all circumstances where the phenylamino intermediate is stable for an extended amount of time, its N atom is bonded to two Sn atoms; in addition, this pair of Sn atoms is bonded together, which differs from the intermetallic bulk catalyst structure. *Ab initio* MD simulations show that at 1200 K—an arbitrary temperature set artificially high enough to speed up the simulations *in silico*, using Pd_2Sn catalysts leads to nitrosobenzene and its hydrogenation products, with chemical formula C_6H_nNO (n = 5 to 10). The mechanism of this reaction involves hydrogenation of one of the two oxygen atoms in nitrobenzene, with subsequent removal of the newly formed OH group. Increasing the temperature to 1500 K results in removal of the second oxygen atom; in this case, most of the product is aniline (C_6H_7N), but there is still a significant amount of phenylamino radical present. Simulations with Au clusters as catalysts show a much smaller amount of phenylamino intermediate, which was observed in only one simulation at 2000 K. Simulations with Pt clusters as catalysts show the hydrogenation process is much quicker than over Au or Pd_2Sn catalysts. Most notably, various aniline hydrogenation products, with chemical formula C_6H_nN (n = 9,11, *etc.*) dominate over Pt catalysts, with a minimal amount of phenylamino present.

The aforementioned *ab initio* MD simulations are computationally expensive and limited to very small systems and short time scales. Recently, potentials that can be trained by machine

learning were developed that can speed up the MD simulations by several orders of magnitude.[77,80,81,82,83,84,85] One such approach exploits a deep neural network (DeePMD) framework, which has been applied for various applications in physical and materials science. Here, we employ the DeePMD framework for what we believe is the first such analysis of a heterogeneous catalytic system.

Specifically, we use clusters with total number of atoms N = 192—in the case of Pd_2Sn, this corresponds to 128 Pd's and 64 Sn's—and 32 molecules of nitrobenzene, 32 of ethanol, and 384 of H_2 in a periodic cube of side length 3 nm to analyze nitroarene reduction with 10 ps simulations. We can discern several trends not evident in our *ab initio* MD simulations. First, the ability to dissociate H_2 into chemisorbed H is very strong on pure Pd, but intermediate on Pd_2Sn, and very weak on pure Sn catalysts. Second, at the temperature where around half of the nitrobenzene reactants are converted, the most populous N containing species is nitrosobenzene (C_6H_5NO) on Pd_2Sn (2000 K), N-oxido-N-phenylhydroxylamine ($C_6H_6NO_2$) on Pd (2000 K), and phenylamino radical ($C_6H_5N•$) on Sn catalysts (1400 K) (Figure 7). Further, while the initial conversion of nitrobenzene is very fast on Sn catalysts, hydrogenation of O adatoms is slower on Sn compared to that on Pd and Pd_2Sn catalysts. This impedes further conversion of nitrobenzene after the catalyst is covered by O adatoms or partially oxidized. At these temperatures, however, the final products may not be indicative of real experimental data near room temperature.

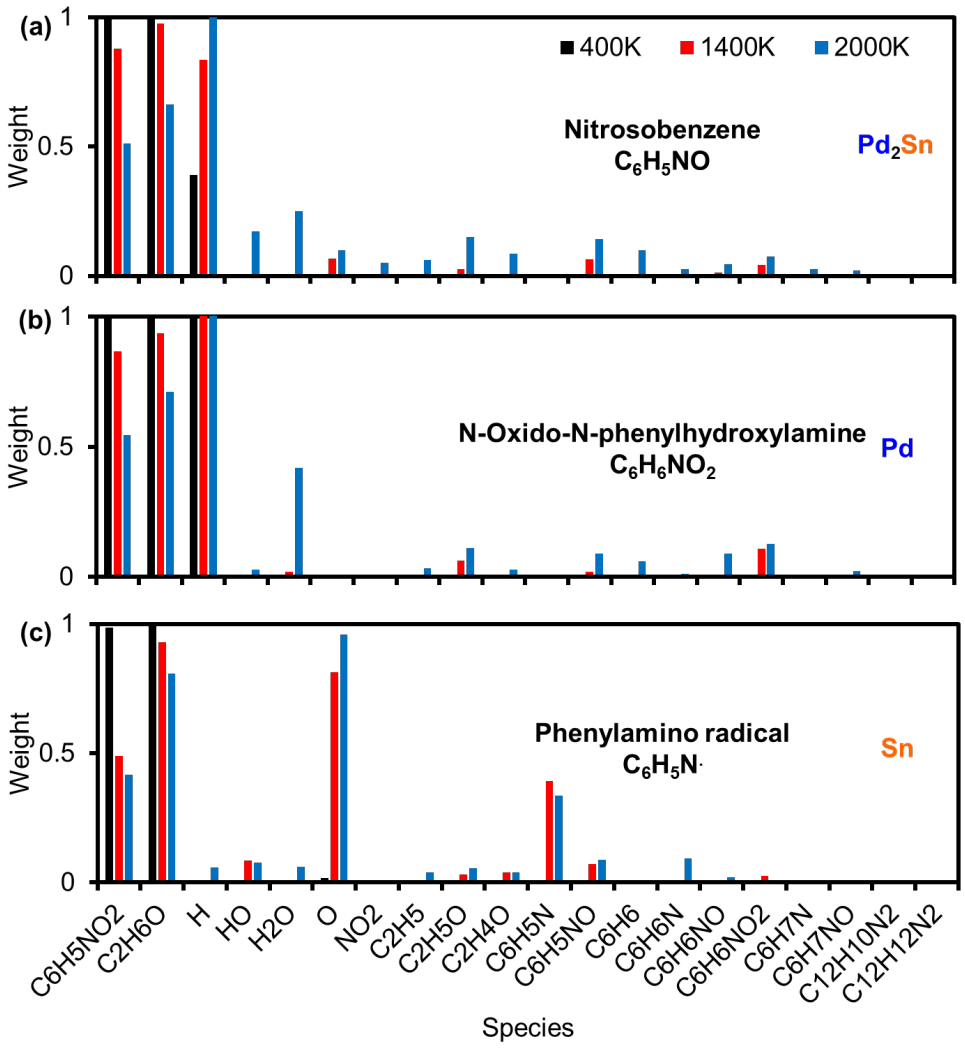

Figure 7. Selected results of simulations with (a) Pd_2Sn, (b) Pd, and (c) Sn nanocatalysts at various temperatures (see details in Methods). The major products at 50% nitrobenzene conversion are displayed in bold in each case.

Longer simulations (up to 100 ps) lead to similar observations. At temperatures with 50% conversion, the most populous nitrogen species is nitrosobenzene (C_6H_5NO) on Pd_2Sn (1200 K), N-oxido-N-phenylhydroxylamine ($C_6H_6NO_2$) on Pd (1400 K), and phenylamino radical (C_6H_5N•) on Sn nanocatalysts (800 K) (Figure 8). While these temperatures are still much higher than R.T., the results are consistent with simulations run for $^1/_{10}$ shorter time. Further

examination of the simulation results shows that ethanol does not directly participate in the reaction. Because it also does not adsorb to the catalyst significantly, we ignored ethanol in further analyses.

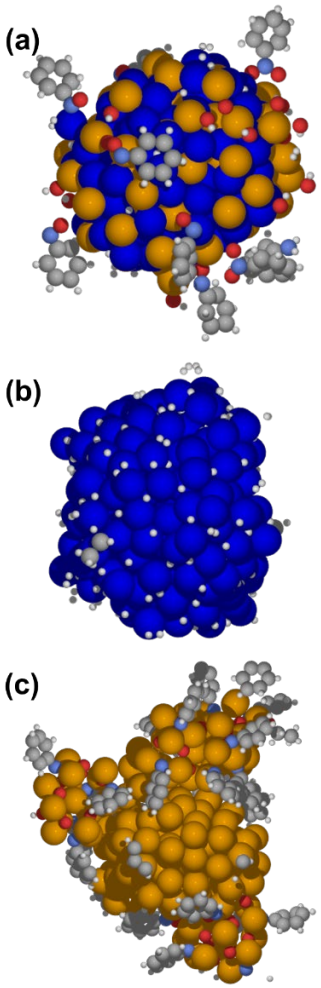

Figure 8. Configurations of catalysts and adsorbed molecules obtained from 100 ps simulations at 50% conversion temperatures: (a) 1200 K Pd_2Sn (b) 1400 K Pd, and (c) 800 K Sn catalysts. (Initially with 32 molecules of nitrobenzene, 32 of ethanol, and 384 of H_2) (See S.I. as well as Methods)

DeePMD Reaction Pathway Analysis. Even with machine learned potentials, long enough simulations at realistic temperatures are nearly impossible. Therefore, we tailored the simulations to gain more insight into the intermediate steps of the reactions. Using Pd_2Sn as a catalyst, our initial simulations for nitrobenzene reduction show that nitrosobenzene is the most populous product between t = 10 to 100 ps at T < 1200 K. Simulations starting with nitrosobenzene and H_2 molecules as reactants initially yield only phenylamino radical (C_6H_5N•), along with nitrosobenzene dimers ($C_{12}H_{10}N_2O_2$). Azoxybenzene ($C_{12}H_{10}N_2O$) starts to appear around T = 1200 K, while aniline (C_6H_7N) formation remains minimal. This shows Pd_2Sn catalysts have a clear selectivity toward azoxybenzene ($C_{12}H_{10}N_2O$) when the initial reactant is nitrosobenzene (C_6H_5NO). In other words, simulations show that the reaction from C_6H_5NO to C_6H_5N• and O on Pd_2Sn catalysts is very facile, and that this is followed by reaction of C_6H_5N• and C_6H_5NO to produce $C_{12}H_{10}N_2O$. Notably, azobenzene ($C_{12}H_{10}N_2$) is not observed, demonstrating that azoxybenzene ($C_{12}H_{10}N_2O$) is a necessary intermediate for the formation of any final azobenzene.

With azoxybenzene ($C_{12}H_{10}N_2O$) and H_2 as reactants, we start to observe azobenzene ($C_{12}H_{10}N_2$) at T = 1200 K. However, the conversion rate is surprisingly low, much less than the rates for oxygen detachment from nitrobenzene and nitrosobenzene. Further analysis of these data show that the conversion rate of azoxybenzene can be fitted to an Arrhenius equation with a barrier of 0.94 eV and a prefactor of 6.4×10^{13} s^{-1}, which can be extrapolated to 0.01 s^{-1} at 300 K, in reasonable agreement with experiments.

Above, we concluded that when a Pd catalyst is used, the first reaction product is *N*-oxido-*N*-phenylhydroxylamine ($C_6H_6NO_2$). Simulations starting from phenylhydroxylamine and H_2 show nitrosobenzene (C_6H_5NO) is the main product below 1000 K, aside from that converted back to

nitrobenzene ($C_6H_5NO_2$). Some N,N-dihydroxyaniline ($C_6H_7NO_2$) can also be found at low T. When starting from nitrosobenzene and H_2 for a Pd catalyst, the main product below 1000 K is N-oxidoaniline (C_6H_6NO), with some nitrosobenzene dimers ($C_{12}H_{10}N_2O_2$) also present. Starting with N-oxidonaniline (C_6H_6NO) and H_2, the first product is phenylhydroxylamine (C_6H_7NO). Starting from phenylhydroxylamine, phenylamino radical (C_6H_5N•) quickly forms by detaching one HO• radical. Subsequently, this can be easily hydrogenated to aniline (C_6H_7N).

Also mentioned above, in the presence of the O-covered Sn catalyst, nitrobenzene ($C_6H_5NO_2$) is very quickly converted to phenylamino radical (C_6H_5N•) and nitrosobenzene (C_6H_5NO). Further reaction is inhibited by the oxygen, because Sn catalysts can neither accept more oxygen from nitrobenzene, nor dissociate any H, unless the surface oxygen is hydrogenated. Direct simulation on a Sn cluster with O_2 and H_2 molecules yields a barrier for oxygen hydrogenation of 0.91 eV and a prefactor of 10^{12} s^{-1}. Once oxygen is removed, hydrogenation proceeds similarly to that over Pd_2Sn catalysts.

With insight from DeePMD simulations, it is clear that nitrosobenzene (C_6H_5NO) forms easily from nitrobenzene and thus is not a limiting step with any of the nanocatalysts tested. Further, nitrosobenzene is reduced to phenylamino radical (C_6H_5N•) over Pd_2Sn, whereas it is hydrogenated to N-oxidoaniline (C_6H_6NO) over Pd catalysts. Starting with nitrobenzene ($C_6H_5NO_2$) over either Pd or Pd_2Sn catalysts, there is also a reaction pathway going through N-oxido-N-phenylhydroxylamine ($C_6H_6O_2$), N,N-dihydroxyaniline ($C_6H_7NO_2$), and N-oxidoaniline (C_6H_6NO). N-oxidoaniline is then converted to aniline (C_6H_7N) through the aforementioned pathway with Pd nanocatalysts, allowing some aniline production on Pd_2Sn catalysts starting from nitrobenzene. However, starting with nitrosobenzene, this pathway is blocked, and thus aniline production is blocked at low temperature, in agreement with our experimental

observations. In summary, there are two pathways for hydrogenation of nitrobenzene with Pd catalysts, both leading to aniline. The first is through nitrosobenzene, and the other is through N,N-dihydroxyaniline. On Pd_2Sn nanocatalysts, the pathway through nitrosobenzene leads to azoxybenzene and azobenzene, while the pathway through N,N-dihydroxyaniline may lead to aniline at sufficiently high temperatures.

CONCLUSIONS

In summary, we find that a majority of the intermetallic nanoparticle catalysts tested—namely, Pd_2Ge, Pd_2Sn, Pd_3Sn_2, and PtSn nanoparticles—favor the indirect condensation pathway and are selective for azoxybenzene. The only exception are Pd_3Pb nanoparticles, which prefer the direct pathway and are selective for aniline. Interestingly, Pd_3Pb nanoparticles are also unique among these nanocatalysts in adopting a face centered cubic (fcc) structure, a feature shared with monometallic Au, Pd, and Pt nanoparticles, and Pd_xSn_{1-x} nanoalloys, all of which are also selective for aniline. In all cases studied, the observed turnover numbers are significantly higher than one, which attests to the catalytic nature of the intermetallic nanoparticles. Maximum turnover frequencies are one to three orders of magnitude faster than those of other unsupported monometallic and alloyed nanocatalysts, and comparable to those of nano Au on TiO_2. Among the different intermetallic nanocatalyst compositions, the observed order of activity is: Pd_3Pb (highest) > Pd_3Sn_2 > Pd_2Sn > Pd_2Ge > PtSn. In other words, for a given set of group 10 metal-based intermetallic nanoparticles, moving down group 14—using a heavier tetrel—increases the catalytic activity.

While standard DFT analysis of the reaction on low-index single-crystal surfaces fails to explain the selectivity of intermetallic nanocatalysts, *ab initio* Molecular Dynamics (MD)

simulations allow us to observe critical intermediates and discern significant differences among various nanocatalysts. Machine learned potentials using a deep neural network (DeePMD), which speed up the simulations by several orders of magnitude show that: (1) the ability to chemisorb H_2 is very strong on Pd, intermediate on Pd_2Sn, and very weak on pure Sn nanoparticles, (2) at 50% conversion temperatures, the most populous N containing species are nitrosobenzene on Pd_2Sn, N-oxido-N-phenylhydroxylamine on Pd, and phenylamino radical on Sn nanoparticles, and (3) while initial conversion is very fast on Sn nanoparticles, hydrogenation of O adatoms is slow, impeding further conversion. DeePMD simulations tailored to gain more insight into the intermediate steps of the reactions show that: (4) nitrosobenzene formation from nitrobenzene is easy and not a limiting step with any of the nanocatalysts tested, (5) reaction from nitrosobenzene to phenylamine radical and O on Pd_2Sn nanoparticles is facile, and this is followed by reaction with nitrosobenzene to produce azoxybenzene, and (6) nitrosobenzene is further reduced to phenylamino radical or N-oxidoaniline over Pd nanoparticles, both of which can be further reduced to aniline. We hope that this contribution will continue to motivate additional studies and catalytic applications of highly selective binary and other more complex intermetallic nanomaterials.

ASSOCIATED CONTENT

Supporting Information. Additional synthesis and catalysis schemes, catalyst stability and recycling data for Pd_2Sn, a comparison of activity and selectivity for nitrobenzene and p-nitrotoluene reduction with different nanoparticle catalysts and reaction times, UV-VIS absorption data of different catalysis products, additional computational data, mechanistic pathways, and partial simulation movie.

Author Contributions

The manuscript was written through contributions of all authors. All authors have given approval to the final version of the manuscript.

Notes

The authors declare no competing financial interest.

ACKNOWLEDGMENT

J.V. thanks the U.S. National Science Foundation for a grant from the Division of Chemistry, Macromolecular, Supramolecular, and Nanochemistry Program (1905066). D.-J.L performed the theoretical analysis and computations in this work, and was supported by the U.S. Department of Energy (USDOE), Office of Basic Energy Sciences, Division of Chemical Sciences, Geosciences, and Biosciences through the Ames Laboratory Chemical Physics program, at Ames Laboratory which is operated for the USDOE by Iowa State University under Contract No. DE-AC02- 07CH11358. We thank Jim Evans for valuable discussions.

REFERENCES

[1] Furukawa, S.; Komatsu, T. Intermetallic Compounds: Promising Inorganic Materials for Well-Structured and Electronically Modified Reaction Environments for Efficient Catalysis. *ACS Catal.* **2017**, *7*, 735–765.

[2] Yan, Y.; Du, J. S.; Gilroy, K. D.; Yang, D.; Xia, Y.; Zhang, H. Intermetallic Nanocrystals: Syntheses and Catalytic Applications. *Adv. Mater*. **2017**, *29*, 1605997-1–29.

[3] Marakatti, V. S.; Peter, S. C. Synthetically Tuned Electronic and Geometrical Properties of Intermetallic Compounds as Effective Heterogeneous Catalysts. *Prog. Solid State Chem*. **2018**, *52*, 1–30.

[4] Dasgupta, A.; Rioux, R. M. Intermetallics in Catalysis: An Exciting Subset of Multimetallic Catalysts. *Catal. Today* **2019**, *330*, 2–15.

[5] Yang, Y.; Wei, M. Intermetallic Compound Catalysts: Synthetic Scheme, Structure Characterization and Catalytic Application. *J. Mater. Chem. A* **2020**, 8, 2207–2221.

[6] Zhou, M.; Li, C.; Fang, J. Noble-Metal Based Random Alloy and Intermetallic Nanocrystals: Syntheses and Applications. *Chem. Rev*. **2021**, *121*, 736−795.

[7] Xiao, W.; Lei, W.; Gong, M.; Xin, H. L.; Wang, D. Recent Advances of Structurally Ordered Intermetallic Nanoparticles for Electrocatalysis. *ACS Catal.* **2018**, *8*, 3237−3256.

[8] Rößner, L.; Armbrüster, M. Electrochemical Energy Conversion on Intermetallic Compounds: A Review. *ACS Catal.* **2019**, *9*, 2018−2062.

[9] Kim, H. Y.; Joo, S. H. Recent Advances in Nanostructured Intermetallic Electrocatalysts for Renewable Energy Conversion Reactions. *J. Mater. Chem. A* **2020**, *8*, 8195–8217.

[10] Komatsu, T.; Furukawa, S. Selective Hydrogenation Catalyzed by Intermetallic Compounds. *J. Japan Pet. Inst.* **2020**, *63*, 336–344.

[11] Luo, Z.; Ibáñez, M.; Antolín, A. M.; Genç, A.; Shavel, A.; Contreras, S.; Medina, F.; Arbiol, J.; Cabot, A. Size and Aspect Ratio Control of Pd_2Sn Nanorods and Their Water Denitration Properties. *Langmuir* **2015**, *31*, 3952–3957.

[12] Luo, Z.; Lu, J.; Flox, C.; Nafira, R.; Genç, A.; Arbiol, J.; Llorca, J.; Ibáñez, M.; Morante, J. R.; Cabot, A. Pd_2Sn [010] Nanorods as a Highly Active and Stable Ethanol Oxidation Catalyst. *J. Mater. Chem. A* **2016**, *4*, 16706–16713.

[13] Wang, C.; Wu, Y.; Wang, X.; Zou, L.; Zou, Z.; Yang, H. Low Temperature and Surfactant-Free Synthesis of Pd_2Sn Intermetallic Nanoparticles for Ethanol Electro-Oxidation. *Electrochim. Acta* **2016**, *220*, 628–634.

[14] Yu, X.; Liu, J.; Li, J.; Luo, Z.; Zuo, Y.; Xing, C.; Llorca, J.; Nasiou, D.; Arbiol, J.; Pan, K., et al. Phosphorous Incorporation in Pd_2Sn Alloys for Electrocatalytic Ethanol Oxidation. *Nano Energy* **2020**, *77*, 105116-1–10.

[15] Liang, L.; Li, S.; Chen, Y.; Liu, X.; Wang, T.; Han, J.; Jiao, S.; Cao, R.; Li, Q. Ultrathin and Defect-Rich Intermetallic Pd_2Sn Nanosheets for Efficient Oxygen Reduction Electrocatalysis. *J. Mater. Chem. A* **2020**, *8*, 15665–15669.

[16] Zhang, J.; Shao, Q.; Zhang, Y.; Sai, S.; Feng, Y.; Huang, X. Promoting the Direct H_2O_2 Generation Catalysis by Using Hollow Pd–Sn Intermetallic Nanoparticles. *Small* **2018**, *14*, 1703990-1–7.

[17] Nafria, R.; Luo, Z.; Ibáñez, M.; Martí-Sànchez, S.; Yu, X.; de la Mata, M.; Llorca, J.; Arbiol, J.; Kovalenko, M. V.; Grabulosa, A., et al. Growth of Au−Pd_2Sn Nanorods via Galvanic Replacement and Their Catalytic Performance on Hydrogenation and Sonogashira Coupling Reactions. *Langmuir* **2018**, *34*, 10634−10643.

[18] Chen, M.; Yan, Y.; Gebre, M.; Ordonez, C.; Liu, F.; Qi, L.; Lamkins, A.; Jing, D.; Dolge, K.; Zhang, B., et al. Thermal Unequilibrium of PdSn Intermetallic Nanocatalysts: From *in situ* Tailored Synthesis to Unexpected Hydrogenation Selectivity. *Angew. Chem. Int. Ed.* **2021**, *60*, 2−11.

[19] Li, F.; Xue, Q.; Ma, G.; Li, S.; Hu, M.; Yao, H.; Wang, X.; Chen, Y. Formic Acid Decomposition-Inhibited Intermetallic Pd_3Sn_2 Nanonetworks for Efficient Formic Acid Electrooxidation. *J. Power Sources* **2020**, *450*, 227615-1−9.

[20] Sarkar, S.; Jana, R.; Suchitra; Waghmare, U. V.; Kuppan, B.; Sampath, S.; Peter, S. C. Ordered Pd_2Ge Intermetallic Nanoparticles as Highly Efficient and Robust Catalyst for Ethanol Oxidation. *Chem. Mater*. **2015**, *27*, 7459–7467.

[21] Chen, J.-Y.; Jheng, S.-L.; Chan, C.-Y.; Tuan, H.-Y. Morphology Controlled Synthesis of Pd_2Ge Nanostructures and their Shape-Dependent Catalytic Properties for Hydrogen Evolution Reaction. *Int. J. Hydrog. Energy* **2019**, *44*, 12958−12970.

[22] Cui, Z.; Chen, H.; Zhao, M.; DiSalvo, F. J. High-Performance Pd_3Pb Intermetallic Catalyst for Electrochemical Oxygen Reduction. *Nano Lett.* **2016**, *16*, 2560−2566.

[23] Tang, C.; Zhang, N.; Ji, Y.; Shao, Q.; Li, Y.; Xiao, X.; Huang, X. Fully Tensile Strained Pd_3Pb/Pd Tetragonal Nanosheets Enhance Oxygen Reduction Catalysis. *Nano Lett.* **2019**, *19*, 1336−1342.

[24] Gamler, J. T. L.; Shin, K.; Ashberry, H. M.; Chen, Y.; Bueno, S. L. A.; Tang, Y.; Henkelman, G.; Skrabalak, S. E. Intermetallic Pd_3Pb Nanocubes with High Selectivity for the 4-Electron Oxygen Reduction Reaction Pathway. *Nanoscale* **2020**, *12*, 2532–2541.

[25] Guo, J.; Wang, H.; Xue, F.; Yu, D.; Zhang, L.; Jiao, S.; Liu, Y.; Lu, Y.; Liu, M.; Ruan, S., et al. Tunable Synthesis of Multiply Twinned Intermetallic Pd_3Pb Nanowire Networks Toward Efficient N_2 to NH_3 Conversion. *J. Mater. Chem. A* **2019**, *7*, 20247–20253.

[26] Jana, R.; Subbarao, U.; Peter, S. C. Ultrafast Synthesis of Flower-like Ordered Pd_3Pb Nanocrystals with Superior Electrocatalytic Activities Towards Oxidation of Formic Acid and Ethanol. *J. Power Sources* **2016**, *301*, 160−169.

[27] Gunji, T.; Noh, S. H.; Tanabe, T.; Han, B.; Nien, C. Y.; Ohsaka, T.; Matsumoto, F. Enhanced Electrocatalytic Activity of Carbon-Supported Ordered Intermetallic Palladium−Lead (Pd_3Pb) Nanoparticles toward Electrooxidation of Formic Acid. *Chem. Mater*. **2017**, *29*, 2906−2913.

[28] Yu, X.; Luo, Z.; Zhang, T.; Tang, P.; Li, J.; Wang, X.; Llorca, J.; Arbiol, J.; Liu, J.; Cabot, A. Stability of Pd_3Pb Nanocubes during Electrocatalytic Ethanol Oxidation. *Chem. Mater.* **2020**, *32*, 2044–2052.

[29] Furukawa, S.; Suga, A.; Komatsu, T. Highly Efficient Aerobic Oxidation of Various Amines Using Pd_3Pb Intermetallic Compounds as Catalysts. *Chem. Commun.* **2014**, *50*, 3277−3280.

[30] Marakatti, V. S.; Sarma, S. Ch.; Sarkar, S.; Krajčí, M.; Gaigneaux, E. M.; Peter, S. C. Synthetically Tuned Pd-Based Intermetallic Compounds and their Structural Influence on the O_2 Dissociation in Benzylamine Oxidation. *ACS Appl. Mater. Interfaces* **2019**, *11*, 37602−37616.

[31] Hoseini, S. J.; Barzegar, Z.; Bahrami, M.; Roushani, M.; Rashidi, M. Organometallic Precursor Route for the Fabrication of PtSn Bimetallic Nanotubes and Pt_3Sn/Reduced-Graphene Oxide Nanohybrid Thin Films at Oil–Water Interface and Study of their Electrocatalytic Activity in Methanol Oxidation. *J. Organomet. Chem.* **2014**, *769*, 1–6.

[32] Chen, W.; Lei, Z.; Zeng, T.; Wang, L.; Cheng, N.; Tan, Y.; Mu, S. Structurally Ordered PtSn Intermetallic Nanoparticles Supported on ATO for Efficient Methanol Oxidation Reaction. *Nanoscale* **2019**, *11*, 19895–19902.

[33] Maligal-Ganesh, R. V.; Xiao, C.; Goh, T. W.; Wang, L.-L.; Gustafson, J.; Pei, Y.; Qi, Z.; Johnson, D. D.; Zhang, S.; Tao, F., et al. A Ship-in-a-Bottle Strategy to Synthesize Encapsulated Intermetallic Nanoparticle Catalysts: Exemplified for Furfural Hydrogenation. *ACS Catal.* **2016**, *6*, 1754–1763.

[34] Ding, J.; Bu, L.; Zhang, N.; Yao, J.; Huang, Y.; Huang, X. Facile Synthesis of Ultrathin Bimetallic PtSn Wavy Nanowires by Nanoparticle Attachment as Enhanced Hydrogenation Catalysts. *Chem. Eur. J.* **2015**, *21*, 3901–3905.

[35] Pei, Y.; Qi, Z.; Goh, T. W.; Wang, L.-L.; Maligal-Ganesh, R. V.; MacMurdo, H. L.; Zhang, S.; Xiao, C.; Li, X.; Tao, F., et al. Intermetallic Structures with Atomic Precision for Selective Hydrogenation of Nitroarenes. *J. Catal*. **2017**, *356*, 307–314.

[36] Dietrich, C.; Hähsler, M.; Wang, W.; Kübel, C.; Behrens, S. Designing Structurally Ordered Pt/Sn Nanoparticles in Ionic Liquids and their Enhanced Catalytic Performance. *ChemNanoMat* **2020**, *6*, 1854–1862.

[37] Deng, L.; Miura, H.; Shishido, T.; Hosokawa, S.; Teramura, K.; Tanaka, T. Dehydrogenation of Propane over Silica-Supported Platinum–Tin Catalysts Prepared by Direct Reduction: Effects of Tin/Platinum Ratio and Reduction Temperature. *ChemCatChem* **2014**, *6*, 2680–2691.

[38] Furukawa, S.; Tamura, A.; Ozawa, K.; Komatsu, T. Catalytic Properties of Pt-based Intermetallic Compounds in Dehydrogenation of Cyclohexane and *n*-Butane. *Appl. Catal. A* **2014**, *469*, 300–305.

[39] Schranck, J.; Tlili, A. Transition-Metal-Catalyzed Monoarylation of Ammonia. *ACS Catal*. **2018**, *8*, 405−418.

[40] Corma, A.; Serna, P. Chemoselective Hydrogenation of Nitro Compounds with Supported Gold Catalysts. *Science* **2006**, *313*, 332–334.

[41] Boronat, M.; Concepción, P.; Corma, A.; González, S.; Illas, F.; Serna, P. A Molecular Mechanism for the Chemoselective Hydrogenation of Substituted Nitroaromatics with Nanoparticles of Gold on TiO_2 Catalysts: A Cooperative Effect between Gold and the Support. *J. Am. Chem. Soc.* **2007**, *129*, 16230–16237.

[42] Serna, P.; Corma, A. Transforming Nano Metal Nonselective Particulates into Chemoselective Catalysts for Hydrogenation of Substituted Nitrobenzenes. *ACS Catal*. **2015**, *5*, 7114−7121.

[43] Grirrane, A.; Corma, A.; García, H. Gold-Catalyzed Synthesis of Aromatic Azo Compounds from Anilines and Nitroaromatics. *Science* **2008**, *322*, 1661–1664.

[44] Makosch, M.; Sá, J.; Kartusch, C.; Richner, G.; van Bokhoven, J. A.; Hungerbühler, K. Hydrogenation of Nitrobenzene Over Au/MeO_x Catalysts—A Matter of the Support. *ChemCatChem* **2012**, *4*, 59–63.

[45] Liu, X.; Ye, S.; Liu, Y.-M.; Cao, Y.; K.-N., F. Mild, Selective and Switchable Transfer Reduction of Nitroarenes Catalyzed by Supported Gold Nanoparticles. *Catal. Sci. Technol.* **2013**, *3*, 3200–3206.

[46] Combita, D.; Concepción, P.; Corma, A. Gold Catalysts for the Synthesis of Aromatic Azocompounds from Nitroaromatics in One Step. *J. Catal*. **2014**, *311*, 339–349.

[47] Liu, Q.; Xu, Y.; Qiu, X.; Huang, C.; Liu, M. Chemoselective Hydrogenation of Nitrobenzenes Activated with Tuned Au/h-BN. *J. Catal*. **2019**, *370*, 55–60.

[48] Hong, J. E.; Jung, Y.; Park, Y.; Park, Y. Highly Selective Synthesis of Hydrazoarenes from Nitroarenes via Polystyrene-Supported Au-Nanoparticle-Catalyzed Reduction: Application to Azoarenes, Aminoarenes, and 4,4′-Diaminobiaryls. *ACS Omega* **2020**, *5*, 7576−7583.

[49] Morales-Guio, C. G.; Yuranov, I.; Kiwi-Minsker, L. Highly Selective Catalytic Reduction of Nitro- to Azoarenes under Ambient Conditions. *Top. Catal.* **2014**, *57*, 1526–1532.

[50] Pahalagedara, M. N.; Pahalagedara, L. R.; He, J.; Miao, R.; Gottlieb, B.; Rathnayake, D.; Suib, S. L. Room Temperature Selective Reduction of Nitrobenzene to Azoxybenzene Over Magnetically Separable Urchin-like Ni/Graphene Nanocomposites. *J. Catal.* **2016**, *336*, 41–48.

[51] Lakshminarayana, B.; Manna, A. K.; Satyanarayana, G.; Subrahmanyam, Ch. Palladium Nanoparticles on Silica Nanospheres for Switchable Reductive Coupling of Nitroarenes. *Catal. Lett.* **2020**, *150*, 2309–2321.

[52] Teng, Y.; Wang, X.; Wang, M.; Liu, Q.; Shao, Y.; Li, H.; Liang, C.; Chen, X.; Wang, H. A Schiff-Base Modified Pt Nano-Catalyst for Highly Efficient Synthesis of Aromatic Azo Compounds. *Catalysts* **2019**, *9*, 339-1–10.

[53] Wang, J.; Yu, X.; Shi, C.; Lin, D.; Li, J.; Jin, H.; Chen, X.; Wang, S. Iron and Nitrogen Co-Doped Mesoporous Carbon-Based Heterogeneous Catalysts for Selective Reduction of Nitroarenes. *Adv. Synth. Catal.* **2019**, *361*, 3525–3531.

[54] Yan, H.; Zhao, X.; Guo, N.; Lyu, Z.; Du, Y.; Xi, S.; Guo, R.; Chen, C.; Chen, Z.; Liu, W., et al. Atomic Engineering of High-Density Isolated Co Atoms on Graphene with Proximal-Atom Controlled Reaction Selectivity. *Nat. Commun.* **2018**, *9*, 3197-1–9.

[55] Cao, C.; Song, W. Single-Atom Catalysts for Thermal Heterogeneous Catalysis in Liquid: Recent Progress and Future Perspective. *ACS Materials Lett*. **2020**, *2*, 1653−1661.

[56] Zhao, J.-X.; Chen, C.-Q.; Xing, C.-H.; Jiao, Z.-F.; Yu, M.-T.; Mei, B.-B.; Yang, Y.; Zhang, B.-Y.; Jiang, Z.; Qin, Y. Selectivity Regulation in Au-Catalyzed Nitroaromatic Hydrogenation by Anchoring Single-Site Metal Oxide Promoters. *ACS Catal.* **2020**, *10*, 2837−2844.

[57] Hu, L.; Cao, X.; Chen, L.; Zheng, J.; Lu, J.; Sun, X.; Gu, H. Highly Efficient Synthesis of Aromatic Azos Catalyzed by Unsupported Ultra-Thin Pt Nanowires. *Chem. Commun*. **2012**, *48*, 3445–3447.

[58] Moran, M. J.; Martina, K.; Baricco, F.; Tagliapietra, S.; Manzoli, M.; Cravotto, G. Tuneable Copper Catalysed Transfer Hydrogenation of Nitrobenzenes to Aniline or Azo Derivatives. *Adv. Synth. Catal*. **2020**, *362*, 2689–2700.

[59] Shukla, A.; Singha, R. K.; Sasaki, T.; Adak, S.; Bhandari, S.; Prasad, V. V. D. N.; Bordoloi, A.; Bal, R. Room Temperature Selective Reduction of Nitroarenes to Azoxy Compounds over Ni-TiO_2 Catalyst. *Mol. Catal.* **2020**, *490*, 110943.

[60] Yan, Z.; Xie, X.; Song, Q.; Ma, F.; Sui, X.; Huo, Z.; Ma, M. Tandem Selective Reduction of Nitroarenes Catalyzed by Palladium Nanoclusters. *Green Chem*. **2020**, *22*, 1301–1307.

[61] Zhu, H.; Ke, X.; Yang, X.; Sarina, S.; Liu, H. Reduction of Nitroaromatic Compounds on Supported Gold Nanoparticles by Visible and Ultraviolet Light. *Angew. Chem. Int. Ed*. **2010**, *49*, 9657–9661.

[62] Liu, Z.; Huang, Y.; Xiao, Q.; Zhu, H. Selective Reduction of Nitroaromatics to Azoxy Compounds on Supported Ag–Cu Alloy Nanoparticles Through Visible Light Irradiation. *Green Chem*. **2016**, *18*, 817–825.

[63] Chen, G.-J.; Xin, W.-L.; Wang, J.-S.; Cheng, J.-Y.; Dong, Y.-B. Visible-light Triggered Selective Reduction of Nitroarenes to Azo Compounds Catalysed by Ag@Organic Molecular Cages. *Chem. Commun*. **2019**, *55*, 3586–3589.

[64] Dai, X.; Wei, Q.; Duong, T.; Sun, Y. Selective Transfer Coupling of Nitrobenzene to Azoxybenzene on Rh Nanoparticle Catalyst Promoted by Photoexcited Hot Electrons. *ChemNanoMat* **2019**, *5*, 1000–1007.

[65] Wang, B.; Deng, Z.; Li, Z. Efficient Chemoselective Hydrogenation of Nitrobenzene to Aniline, Azoxybenzene and Azobenzene over CQDs/$ZnIn_2S_4$ Nanocomposites Under Visible Light. *J. Catal*. **2020**, *389*, 241–246.

[66] Zhang, Y.-F.; Mellah, M. Convenient Electrocatalytic Synthesis of Azobenzenes from Nitroaromatic Derivatives Using SmI_2. *ACS Catal.* **2017**, *7*, 8480−8486.

[67] Kumar, G. S.; Neckers, D. C. Photochemistry of Azobenzene-Containing Polymers. *Chem. Rev.* **1989**, *89*, 1915–1925.

[68] Huang, J. M.; Kuo, J. F.; Chen, C. Y. Studies on Mesomorphic Behaviors of Segmented Azoxy Polyester Containing Polyoxyethylene. *J. Appl. Polym*. *Sci.* **1995**, *55*, 1217–1229.

[69] Ikeda, T.; Tsutsumi, O. Optical Switching and Image Storage by Means of Azobenzene Liquid-Crystal Films. *Science* **1995**, *268*, 1873–1875.

[70] Hamon, F.; Djedaini-Pilard, F.; Barbot, F.; Len, C. Azobenzenes—Synthesis and Carbohydrate Applications. *Tetrahedron* **2009**, *65*, 10105–10123.

[71] Bandara, H. M. D.; Burdette, S. C. Photoisomerization in Different Classes of Azobenzene. *Chem. Soc. Rev*. **2012**, *41*, 1809–1825.

[72] Mahata, A.; Rai, R. K.; Choudhuri, I.; Singh, S. K.; Pathak, B. Direct *vs.* Indirect Pathway for Nitrobenzene Reduction Reaction on a Ni Catalyst Surface: A Density Functional Study. *Phys. Chem. Chem. Phys*. **2014**, *16*, 26365−26374

[73] Zhang, L.; Shao, Z.-J.; Cao, X.-M.; Hu, P. Interface-Tuned Selective Reductive Coupling of Nitroarenes to Aromatic Azo and Azoxy: A First-Principles-Based Microkinetics Study. *Phys. Chem. Chem. Phys.* **2019**, *21*, 12555−12565.

[74] Daniels, C. L.; Knobeloch, M.; Yox, P.; Adamson, M. A. S.; Chen, Y.; Dorn, R. W.; Wu, H.; Zhou, G.; Fan, H.; Rossini, A. J., et al. Intermetallic Nanocatalysts from Heterobimetallic Group 10−14 Pyridine-2-Thiolate Precursors. *Organometallics* **2020**, *39*, 1092−1104.

[75] Wang, A.-L.; Zhu, L.; Yun, Q.; Han, S.; Zeng, L.; Cao, W.; Meng, X.; Xia, J.; Lu, Q. Bromide Ions Triggered Synthesis of Noble Metal–Based Intermetallic Nanocrystals. *Small* **2020**, *16*, 2003782-1–7.

[76] Du, W.; Mackenzie, K. E.; Milano, D. F.; Deskins, N. A.; Su, D.; Teng, X. Palladium−Tin Alloyed Catalysts for the Ethanol Oxidation Reaction in an Alkaline Medium. *ACS Catal.* **2012**, *2*, 287−297.

[77] Dontgen, M.; Przybylski-Freund, M.-D.; Kröger, L. C.; Kopp, W. A.; Ismail, A. E.; Leonhard, K. Automated Discovery of Reaction Pathways, Rate Constants, and Transition States Using Reactive Molecular Dynamics Simulations. *J. Chem. Theory Comp.* **2015**, *11*, 2517–2524.

[78] *Inorganic Crystal Structure Database*, version 4.6.0; FIZ Karlsruhe: Karlsruhe, Germany, 2021.

[79] Fountoulaki, S.; Daikopoulou, V.; Gkizis, P. L.; Tamiolakis, I.; Armatas, G. S.; Lykakis, I. N. Mechanistic Studies of the Reduction of Nitroarenes by $NaBH_4$ or Hydrosilanes Catalyzed by Supported Gold Nanoparticles. *ACS Catal.* **2014**, *4*, 3504–3511.

[80] Behler, J. Perspective: Machine Learning Potentials for Atomistic Simulations. *J. Chem. Phys.* **2016**, *145*, 170901-1–9.

[81] Wang, H.; Zhang, L.; Han, J.; Weinan, E. DeePMD-kit: A Deep Learning Package for Many-body Potential Energy Representation and Molecular Dynamics. *Comput. Phys. Commun.* **2018**, *228*, 178–184.

[82] Behler, J.; Lorenz, S.; Reuter, K. Representing Molecule-Surface Interactions with Symmetry-Adapted Neural Networks *J. Chem. Phys.* **2007**, *127*, 014705-1–11.

[83] Han, J.; Zhang, L.; Car, R.; Weinan, E. Deep Potential: A General Representation of a Many-Body Potential Energy Surface. *Commun. Comput. Phys.* **2018**, *23*, 629–639.

[84] Zhang, L.; Han, J.; Wang, H.; Car, R.; Weinan, E. Deep Potential Molecular Dynamics: A Scalable Model with the Accuracy of Quantum Mechanics. *Phys. Rev. Lett.* **2018**, *120*, 143001-1–6.

[85] Jinnouchi, R.; Karsai, F.; Kresse, G. On-the-fly Machine Learning Force Field Generation: Application to Melting Points. *Phys. Rev. B* **2019**, *100*, 014105-1–15.

TOC Graphic